Imaging of laser-generated ultrasonic waves in silicon

A. G. Every* and Wolfgang Sachse
Department of Theoretical and Applied Mechanics, Cornell University, Ithaca, New York 14853
(Received 20 December 1990; revised manuscript received 22 April 1991)

In this paper we report the results of experiments that we have carried out on single-crystal specimens of silicon using a scanned ultrasonic point-source–point-receiver technique. Transient waves are generated thermoelastically using the focused beam of a Q-switched neodymium-doped yttrium aluminum garnet laser, which is scanned across one face of the disk-shaped sample, and the waves are detected with a small-aperture lead zirconate-titanate piezoelectric transducer mounted on the opposite face. We present the results in the form of gray-scale scan images, which display the spatial and time dependence of the radiated wave forms. These scan images contain clearly defined structures due to singularities in the wave field associated with various wave arrivals, including single-pass longitudinal and transverse waves, multipass sequences involving mode conversion on reflection and head waves between the longitudinal and one or both of the transverse modes. A pronounced anisotropy is observed in the amplitudes of the wave arrivals, which is mainly attributable to anisotropy or phonon focusing of the acoustic energy flux. Source directivity has a significant influence on the amplitudes of the longitudinal wave arrivals. The thermoelastic generation mechanism favors the radiation of vertical shear-(SV) type displacements, and for some experimental configurations this leads to a strong slow-quasitransverse-wave signal and the almost complete extinction of the fast-quasitransverse-wave signal, while in other cases the reverse is obtained. Monte Carlo simulations based on ray constructs account well for the various wave arrivals and for the focusing effects. The changes in the scan images arising from the presence of surface damage are interpreted, thereby demonstrating the potential usefulness of scan imaging as a tool for surface characterization.

I. INTRODUCTION

In this paper[1] we report the results of experiments we have carried out on silicon single crystals using a scanned ultrasonic point-source–point-receiver (PS-PR) technique.[2] The ultrasonic waves are generated thermoelastically using the focused beam of a pulsed Q-switched laser, which is scanned across one face of the disk-shaped sample, and the waves are detected with a small-aperture piezoelectric transducer mounted on the opposite face. In contrast to the more common type of ultrasonic experiment, in which plane waves are sent in specific directions through a sample, with the PS-PR technique wide-angle radiation and detection is accomplished. PS-PR wave forms are more complex than plane-wave trains, but in compensation they convey a great deal of information regarding propagation speeds and amplitudes in various directions in the medium, the spatial variation of material properties, and mode conversion at the boundaries, etc. Moreover, all three wave polarizations are, in general, present in these wave forms, which is an added advantage.

We present our results in the form of gray-scale scan images formed by stacking together a large number of wave forms for a closely spaced set of excitation points. These scan images display large amplitude signals in directions where anisotropy focusing (phonon focusing) is predicted to lead to a divergence in the energy flux.[3–6] While phonon focusing caustics are well known in phonon imaging,[7–10] the present investigations provide experimental evidence of these structures for MHz ultrasonic waves. Our results on silicon are in good agreement with the predictions of Monte Carlo simulations of the far-field acoustic intensity based on ray constucts.

Our scan images also contain clearly defined structures due to multipass waves, i.e., waves which have passed several times through the sample with or without undergoing mode conversion on reflection at the surfaces.[11] The source and detector strongly favor the transmission of modes of vertical shear (SV) character, and this plays an important role in determining the relative amplitudes of the various single-pass and multipass modes that are present in the signals.

Head waves can also be clearly discerned in our scan images.[12] Head waves are well known in the study of transient waves in isotropic plates and stratified solids. While the theoretical basis for their existence in anisotropic solids is well established, the observations we report here appear to be unambiguous identification of head waves in single-crystal specimens.[1]

The surfaces of some of our samples are punctured by small laser-generated ablation pits. The presence of this surface damage has a marked effect on the wave forms, leading to strong L-wave enhancement and precursors to the L-wave arrivals in which the direction of displacement is reversed. It is possible to estimate from the time dependence of the signals how far the damage extends into the interior of the sample.

II. EXPERIMENTAL METHOD

The experimental method we have employed is a variation of a broadband ultrasonic point-source–point-

receiver (PS-PR) technique that has been described in greater detail previously.[2] The experiments we are reporting on here have been carried out on three disk-shaped silicon single crystals, whose dimensions, crystallographic orientations, and surface conditions in the region of excitation are listed in Table I.

Ultrasonic waves are generated in the sample using a Q-switched neodymium-doped yttrium aluminum garnet (Nd:YAG) laser, operating at a wavelength of 1.06 μm, which provides pulses of ≈ 4 ns duration and ≈ 10 mJ energy with a duty cycle of about 1 s. The laser beam is focused to a diameter of ≈ 0.5 mm on one face of the sample. The energy density is intentionally kept below the melt threshold (≈ 1 J/mm^2) so that the operating conditions lie within the photoacoustic regime.[13,14] In the case of polished, undamaged samples the light is absorbed within a thin layer at the surface, causing a temperature rise and free thermoelastic expansion normal to the surface. Lateral expansion of the surface layer is, however, constrained by the underlying material, giving rise to lateral compressive stresses. These stresses can be regarded as arising from a pair of orthogonal force dipoles in the surface having a step-function time dependence. The sudden appearance of these forces causes the radiation of transient acoustic waves into the sample.[11] The laser beam is scanned over the face of the sample to provide information on wave propagation for a range of directions.

The theoretical wave forms that are generated by transient forces of the type described above are discussed further in Sec. III. The crucial feature on which our interpretation is based is the existence of sharp spikes or discontinuities in the displacement field that propagate outwards from the source on longitudinal and transverse wave fronts.

The ultrasonic waves are detected with a small-aperture (1.3-mm-diam) lead zirconate-titanate (PZT) piezoelectric transducer mounted on the face opposite the source. The particular sensor we have used was chosen for its relatively high sensitivity. The output voltage signal of the sensor resembles, to some extent, the normal component of the velocity of the sensed surface. The most conspicuous feature of the response is, however, that the arrival of a displacement discontinuity or other sharp feature in the wave form, referred to as a wave arrival, which is accompanied by a large amount of acoustic energy, triggers a damped oscillatory signal (ringing) that persists for up to a microsecond. This behavior is evidenced in all the experimental wave forms presented in this paper. Our main concern here is not with the precise shape of the signal but with the onset of ringing, which coincides with the arrival of a particular wave mode, and with the early amplitude of the signal, which is related to the magnitude of the singularity at the wave front. The onset of ringing can be identified with a precision of ≈ 0.03 μs, indicating that the sensed wave form is principally comprised of Fourier components of frequency $\approx 10^7$ Hz and wavelength $\lambda < 1$ mm. Since λ is much less than the propagation distance, the signal onsets can be considered as far-field effects.

The interpretation of wave-form data is greatly facilitated by stacking together a large number of waveforms obtained from a closely spaced set of excitation points or viewing directions, in a manner akin to a seismogram. The scan images presented in this paper [Figs. 4(a), 5(a), and 6(a)] have been constructed in this manner from 201 wave forms obtained for a set of excitation points 0.2 mm apart along a scan line. A grey scale is used to represent the signal amplitude, with shades of light corresponding to motion of the detector surface towards the source and dark away from the source. This was verified by operating the laser in the ablation regime and observing the sign of the first arrival signal. In these scan images the signal onsets can easily be distinguished from transducer ringing and noise. In the viewing, fluctuations tend to wash out and the wave arrivals are readily identified.

III. TRANSIENT WAVE FORMS

The theory of transient wave forms in solids has attracted a great deal of attention over a number of years and a large body of knowledge has been built up, mainly concerning isotropic solids.[15] A number of problems have succumbed to analytical solution, and efficient computer codes have become available to handle others. Such calculations are of great utility in the interpretation of experimental results in solid mechanics.[11]

Much less is known about the dynamic Green's functions of anisotropic solids. The formal solution of the Green's-function problem for an infinite anisotropic elastic continuum, in terms of Fourier transforms, has been provided by Duff[16] and related questions have been explored by a number of other investigators.[17–19] However, it is only for certain special cases that exact explicit closed-form solutions have been obtained.[20] Up to the present, few detailed numerical results have been published on Green's functions for specific materials and

TABLE I. Experimental samples.

Crystal	*A*	*B*	*C*
Orientation	(100)	(110)	(111)
Thickness	9.906 mm	9.970 mm	10.000 mm
Diameter	7.5 cm	7.5 cm	7.5 cm
Scan-line direction	[001]	[1$\bar{1}$2]	[11$\bar{2}$]
Surface condition	Smooth	Line of ablation pits extending over half of specimen; otherwise smooth.	Single ablation pit; otherwise smooth.

practical testing geometries.[21] The data that is available mainly concerns transversely isotropic solids,[20] and there is no library of theoretical wave forms that we can draw on for comparison with our experimental results on cubic-crystal silicon. It is hoped that the findings reported here will spur further theoretical activity in this direction.

What is known from existing theory is that the wave form generated by the sudden application of a point force consists of a continuous wave punctuated by δ, step function, or other singularities in the displacement field, which propagate outwards from the source on longitudinal and transverse wave fronts. These singularities are far-field features that fall off more slowly [as 1/(distance) or 1/(distance)^2)] than the continuous portion of the wave form, which is a near-field feature. Moreover, the most conspicuous signals in the sensor are triggered by these singularities or wave arrivals. In the interpretation of our results we have consequently not attempted to account for the complete wave forms. Rather, we have confined our attention to signal onsets and amplitudes and their interpretation in terms of wave arrivals.

A. Monte Carlo simulations

Wave front singularities propagate along rays and at any instant of time t are located on a wave surface. The wave surface of an anisotropic solid consists of three sheets belonging to the longitudinal (L), slow-quasitransverse (ST), and fast-quasitransverse (FT) modes (for an isotropic solid all three are spheres and the two transverse sheets coincide). It is common for the transverse sheets to be folded, sometimes in a fairly complicated way, so that in some directions there may be five, seven, or even more wave arrivals. We wish to determine all the wave arrivals during a certain time span for a large number of source-receiver configurations. Given the wave normal of a wave, it is a simple matter to calculate the group velocity of that wave and hence predict its arrival point and time at some surface. The inverse problem of determining all the wave arrivals in a specific direction is, however, not straightforward and, as far as is known, has no analytical solution. It is possible to set up a numerical algorithm to home in on solutions, but there remains the problem of ascertaining when all the solutions have been found. In the most general case, there could be as many as 75 distinct rays in certain directions.[16] The method we outline in this section circumvents these difficulties.

In the ray approximation one deals with plane waves of angular frequency ω and wave vector $\mathbf{k}$, for which the displacement field has the form $\mathbf{u}=\mathbf{U}\exp[ik(\mathbf{n}\cdot\mathbf{x}-vt)]$, where the polarization vector $\mathbf{U}=(U_r)$, wave normal $\mathbf{n}=(n_i)$, and phase velocity $v=\omega/k$ are related by the Christoffel equations[22,23]

$$(C_{rlsm}n_l n_m-\rho v^2\delta_{rs})U_s=0\ , \tag{1}$$

where C_{rlsm} is the elastic modulus tensor (in Voigt contracted notation,[24] $C_{\alpha\beta}$), ρ is the density of the medium, and δ_{rs} is the Kronecker δ. The characteristic equation

$$|C_{rlsm}n_l n_m-\rho v^2\delta_{rs}|=0\ , \tag{2}$$

is cubic in v^2 and determines the directional dependence of the three phase velocities. The energy of a wave travels at the ray or group velocity $\mathbf{V}$ given by

$$\mathbf{V}=\nabla_{\mathbf{k}}\omega(\mathbf{k})=[v(\mathbf{n})-\mathbf{n}\cdot\nabla_{\mathbf{n}}v(\mathbf{n})]\mathbf{n}+\nabla_{\mathbf{n}}v(\mathbf{n})\ . \tag{3}$$

It follows from Eq. (3) that ray vectors are normal to the acoustic slowness surface

$$\Lambda(\mathbf{s})=|C_{rlsm}s_l s_m-\rho\delta_{rs}|=0\ , \tag{4}$$

which is of degree six in the slowness vector $\mathbf{s}=\mathbf{k}/\omega=\mathbf{n}/v$.

Consider a source releasing a short burst of acoustic energy, which is distributed among all mode $\mathbf{n}$'s and the three polarizations. This might, for example, represent a heat pulse comprised of a distribution of thermal phonons or an acoustic emission event of some sort. The acoustic energy spreads outwards in wave packets, each traveling at its respective group velocity $\mathbf{V}$. At time t, these wave packets lie on a wave surface, which is the group velocity or ray surface scaled in size by a factor t. Figure 1 shows a calculated (110)-plane section of the ray surface of silicon[26] constructed from rays associated with an isotropic distribution of wave normals. Each point represents a ray that falls within an angle of 0.03° of the (110) plane. This figure illustrates first of all the complex folding of the wave surface that occurs in anisotropic solids. Secondly, it shows how the rays are crowded together or focused near the cuspidal edges of the folds, indicating that the acoustic energy density is very large there. This effect is well known in phonon transport studies where it is referred to as *phonon focusing*.

A parameter that provides a good measure of anisotropy or phonon focusing is the phonon enhancement or focusing factor A, defined by Maris[3] as

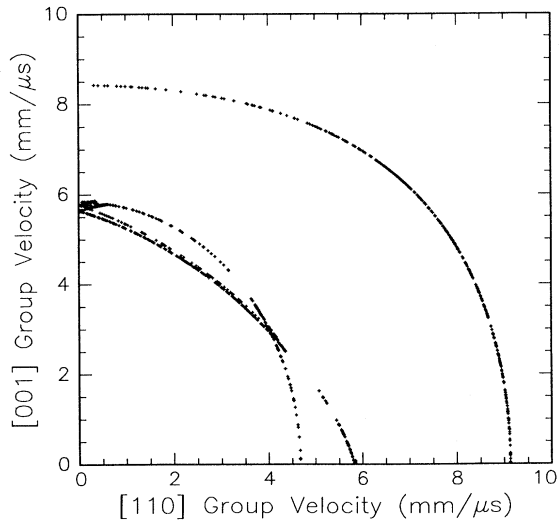

FIG. 1. A (110)-plane section of the ray surface of silicon.

$$A = \delta\Omega_s / \delta\Omega_V \ , \tag{5}$$

where $\delta\Omega_s$ is the infinitesimal solid angle subtended by a small cluster of slowness vectors and $\delta\Omega_V$ is the solid angle subtended by their associated group velocity vectors. The intimate relationship between A and the curvature of the slowness surface has been discussed by a number of authors. It readily follows from the definition of A, that

$$A^{-1} = |s^3 V K| \ , \tag{6}$$

where $K = L_1 L_2$ is the Gaussian curvature and L_1 and L_2 are the two principal curvatures of the slowness surface.

It is common for slowness surfaces of anisotropic solids to be not entirely convext but to possess regions where one or both of the principal curvatures is negative. On the boundaries between these different regions, which map onto the cuspidal edges of the ray surface, the Gaussian curvature is zero and the focusing is therefore infinite. The patterns of caustics that arise in this way are beautifully portrayed in the many phonon images of crystals to be found in the literature.[9] Other factors, such as source directivity and polarization selectivity in the generation process can also influence the directional dependence of the acoustic flux, but in a less dramatic way, without yielding singularities.

In our simulations we employ a Monte Carlo method, randomly generating about 10^6 **n**'s in all directions (taking advantage of crystal symmetry to reduce the actual number of computations). Equations (2) and (3) are used to obtain the group velocity for each mode, and from this the point of arrival and arrival time of that wave at the viewing surface are determined. Using this information, the number of waves of all three polarizations arriving within an acceptance area of 0.1 mm^2 for each of 201 positions in the scan line and 512 discretized time intervals of 16.7 ns is determined. This information is stored in a 201×512 computer array. This process corresponds to the adding of wave intensities, without regard to the phase relationships between the individual waves, and hence yields an energy flux distribution function. The statistical fluctuation due to the finite number of wave arrivals in each bin is about 10%, but when the results are juxtaposed in a scan image, these fluctuations tend to wash out and their visual effect is minimal. The time dependence of the energy flux for each position consists of a number of narrow pulses, each corresponding to an intersection of the source-receiver line with the wave surface. The integrated flux for each of these pulses, i.e., the energy arriving in that pulse, is proportional to the focusing factor and, hence, inversely proportional to $|K|$ for those modes, and it also varies as 1/(distance)^2. This comes out naturally in the statistics of collecting the rays, without having to go through the process of calculating the curvature of the slowness surface. The energy accompanying a singularity is proportional to the square of the magnitude of the singularity, e.g., the size of the displacement discontinuity. To arrive at a quantity that can more closely be compared with our measured wave forms, which are signal amplitude measurements, we therefore take the square root of the computed pulse heights. For signal amplitudes the relevant focusing factor is therefore $A^{1/2}$.

The above procedure permits us to quickly identify all the wave arrivals and their magnitudes for the 201 source-receiver configurations in our scan images. A simulation of first arrivals, based on 10^6 **n**'s using FORTRAN coding and run on a CONVEX C210 supercomputer takes of the order of 2 min of CPU time (the most elaborate calculations we report in this paper, which include multipass and head waves, take about 1 h of CPU time). This method is much simpler than trying to treat the inverse problem directly by identifying all the distinct wave arrivals for each source-receiver configuration and then obtaining the amplitude of each wave arrival by calculating the curvature of the slowness surface for that ray.

B. Source directivity

The nature of the source also has an influence on the amplitudes of the wave arrivals. Source directivity in isotropic solids is fairly well understood,[13,14] but no comprehensive treatment of source directivity in anisotropic solids is available in the literature. Since elastic anisotropy influences source directivity in a quantitative rather than a qualitative way, the theory of source directivity in isotropic solids provides an adequate basis for recognizing source directivity effects in our silicon wave forms and qualitatively understanding how these effects arise. Equations (4.23) and (4.29) of Aki and Richards (Ref. 15) for the response functions of an infinite isotropic elastic solid, allowing the following to be stated.

(1) For a surface thermoacoustic source modeled as a pair of crossed force dipoles with step function time dependence, near epicenter the amplitudes of the longitudinal- (L) and transverse- (T) wave far-field singularities vary approximately as $+\sin^2\theta$ and $-\sin^2\theta$, respectively, where θ is the angular deviation from the epicentral direction. Both therefore vanish at epicenter. The intermediate-field terms in the wave form, however, reach a maximum at epicenter, with the L term being negative and the T term being positive. Mixed-type behavior is not uncommon in experimental situations, has been reported by a number of investigators,[14,25] and is the case also with the results we report in Sec. IV.

(2) A buried thermoacoustic source, modeled as a center of dilatation or three crossed force dipoles, gives rise only to longitudinal waves, with both far- and intermediate-field terms being positive and at a maximum at the epicenter.

C. Multipass waves

We have also incorporated the effects of reflection and mode conversion processes at the surfaces of our specimens in the Monte Carlo simulations. The condition governing the reflection of a plane wave at a plane boundary is that the incoming and three outgoing waves are all phase matched in the boundary. This requires that the slowness vectors of the four waves have the same projection $\mathbf{s}_\parallel$ in the reflecting plane. For given $\mathbf{s}_\parallel$ the component s_3 normal to the plane is determined by Eq. (4),

which has six solutions. Three of these have associated ray or group velocity vectors pointing away from the reflecting surface, and these pertain to the reflected waves. The other three have ray vectors pointing towards the surface, one of these corresponding to the incident wave. The free surface boundary conditions can be used to determine the amplitudes of the outgoing waves, but this has not been done in the present calculations.

The approach we have adopted takes advantage of the fact that the opposite faces of the disk-shaped samples are parallel. A single value of $\mathbf{s}_\parallel$ thus applies throughout any mode conversion sequence. Our method begins by generating a random set of vectors $\mathbf{s}_\parallel$, which are distributed with uniform areal density in the common reflecting plane. For each $\mathbf{s}_\parallel$, the six values of s_3 and associated group velocity vectors are calculated. Three of these, $\mathbf{V}_i^+$, are directed towards the detector surface and three of them, $\mathbf{V}_j^-$, are directed towards the source surface. A single $\mathbf{V}_i^+$ determines the point of arrival and arrival time of a single-pass wave at the detector surface. Similarly, each of the $3^3=27$ combinations of a $\mathbf{V}_i^+$, followed by a $\mathbf{V}_j^-$ and then a $\mathbf{V}_k^+$ determines a three-pass wave arrival. Similarly the $3^5=243$ combinations of the type $\mathbf{V}_i^+\mathbf{V}_j^-\mathbf{V}_k^+\mathbf{V}_l^-\mathbf{V}_m^+$ determine the possible five-pass wave arrivals, etc. Permutations of the $\mathbf{V}_i^+$, $\mathbf{V}_k^+$, and $\mathbf{V}_m^+$ among themselves does not alter the arrival time or the point of arrival, and similarly for the $\mathbf{V}_j^-$ and $\mathbf{V}_l^-$. Hence there are fewer than 243 distinct wave arrivals. Calculating all 243 of them does, on the other hand, simplify the computer algorithm.

As will be discussed later, in the experiments we are reporting on here, only one of the two transverse modes is radiated in any direction. By taking advantage of this fact a considerable reduction in computational time is realized, since there are now only 2^3 three-pass and 2^5 five-pass wave arrivals, etc., and this entails a considerable reduction in the complexity of the pattern of the arriving multipass signals. A particular wave arrival, such as an L wave passage followed by a T wave and then another L wave, may be denoted LTL. Where the reflecting planes are parallel to a crystallographic symmetry plane, the $\mathbf{V}_i^+$ and $\mathbf{V}_j^-$ form mirror-image pairs and the order of the L's and T's in the full sequence does not affect the arrival time or the point of arrival. In this case, the simpler descriptor $2LT$ is adequate. There are thus only four distinct, three-pass wave arrivals $3L$, $2LT$, $L2T$, and $3T$ and six five-pass waves. The computations are also faster when there is a mirror plane, since odd powers of s_3 are absent from the slowness equation, leaving a cubic instead of a sextic equation to be solved.

D. Head waves

When the source is located at (or near) the surface, some of the energy is radiated as head waves. A head wave may be thought of as arising in the following way.[12] An L wave front expanding outwards from the source and skimming the surface generates transverse waves, which provide the compensating tractions to satisfy the boundary conditions. The envelope of these secondary waves forms the head wave front, which is radiated into the interior. Head waves not only trail the L wave front, linking it to the FT and ST waves fronts, but they also link the FT to the ST wave fronts, and in the case of highly anisotropic solids it is possible for a head wave to exist between a transverse wave front and itself. However, it is only the $L\rightarrow$ST and $L\rightarrow$FT head waves that extend inwards close enough to epicenter to be observable in our experiments and that we will consider here.

The head wave front may be regarded as the locus of line segments, each of which joins the tip of an L-ray vector lying in the surface to the tip of a phase-matched T ray pointing into the solid. If the sample's surface is a crystallographic mirror plane, each in-plane L wave has its slowness vector also in the plane, although these slowness and ray vectors are not, in general, parallel. This simplifies the calculation of the head wave front, since qualifying in-plane components of the slowness $\mathbf{s}_\parallel$ are found simply by generating $\mathbf{n}$'s in the plane and obtaining the L phase velocity and hence $\mathbf{s}_\parallel$ from Christoffel's equation. For a surface that is not a symmetry plane, the search for qualifying $\mathbf{s}_\parallel$'s has to be widened to a larger region of the slowness surface. Our (111)-oriented Si crystal is a case in point. We find that the wave normals that yield in-plane ray vectors for this orientation range up to $\approx\pm10°$ from the (111) plane. Because the L sheet of the slowness surface is entirely convex, a single-step application of Newton's method, making use of the angular derivatives of $\mathbf{s}_\parallel$, is able to locate an in-plane L ray with sufficient accuracy.

The calculation of the head wave arrivals in our Monte Carlo simulations is carried out as follows. A large number $\approx10^4$ of qualifying $\mathbf{s}_\parallel$'s is generated, and their accompanying $\mathbf{V}_L(\mathbf{s}_\parallel)$'s and $\mathbf{V}_T(\mathbf{s}_\parallel)$'s computed. For each $\mathbf{s}_\parallel$, the line joining the tips of the vectors $\mathbf{V}_L t$ and $\mathbf{V}_T t$ is a filament of the head wave, which moves steadily outwards with increasing time t. The intersection of this filament with the viewing surface represents a head-wave arrival at that point. The trajectory of this intersection point is computed, and it is determined whether this passes through the acceptance area for any of the source-receiver configurations. When this is the case, based on the arrival time, the appropriate element of the scan-image array is incremented. The sum total of these records forms the simulated heady-wave pattern.

IV. EXPERIMENTAL RESULTS AND INTERPRETATION

Three experimental scan images for silicon are presented in this section. These are itemized in Table I. Figure 2 shows the location of the scan lines in relation to the FT and ST focusing patterns of silicon. These diagrams represent polar plots of the distribution of ray vectors computed for an isotropic distribution of wave normals. The dark regions, where the rays are concentrated, represent directions of strong focusing.

The L branch displays no caustics (this is related to the fact that the slowness equation is of degree six[16]), but there is some variation of intensity with direction. Formulas derived by Maris[3] for the focusing factor A for the

L modes in these high-symmetry directions yield

$$A^{1/2}(\langle 100\rangle)=0.52\ ,$$

$$A^{1/2}(\langle 110\rangle)=1.19\ ,$$

$$A^{1/2}(\langle 111\rangle)=1.48\ ,$$

showing that the focusing is least for the $\langle 100\rangle$ directions.

All our scan images display a strong L-wave signal, but in many cases only one of the two transverse waves is in evidence. This *mode selectivity* is a consequence of the particular crystallographic orientations of our samples and scan lines and the symmetric nature of the source.

The surface and buried thermoacoustic source mechanisms that are expected to play the most important role in our experiments both have approximate axial symmetry about the normal to the sample's surface. For radiation in the direction **n** in an isotropic solid the sagittal plane, containing **n** and the normal to the surface, is a symmetry plane. Hence, only displacements in the sagittal plane can be excited, i.e., vertical shear (SV) waves and not normal displacements, i.e., horizontal shear (SH) waves. It might be expected that this mode selectivity would be absent in anisotropic solids, since the ST and FT modes are, in general, of mixed SH and SV character, but this turns out not to be the case in our experiments. Figures 3(a) and 3(b) depict the polarization patterns of the ST and FT modes of silicon and show the relation of the scan lines to these patterns. Even though these polarization patterns are fairly complex, possessing singularities at the $\langle 100\rangle$ and $\langle 111\rangle$ acoustic axes, the particular scan lines we have selected for measurement encounter fairly simple behavior.

In the case of scan-line A, for instance, the FT modes are to a very high degree SH in character, while the ST modes are SV, so the generation mechanism strongly favors the radiation of ST waves. This bias is reinforced

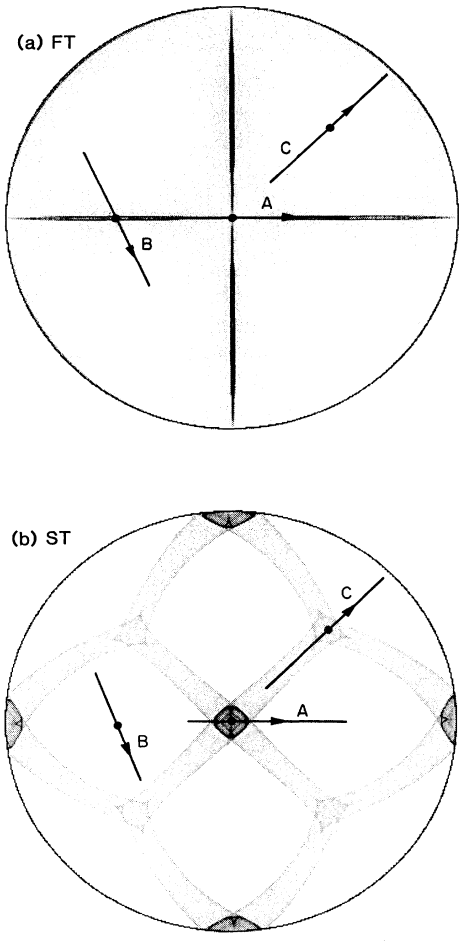

FIG. 2. Polar plots of the anisotropy focusing patterns of silicon: (a) FT modes and (b) ST modes. The approximate trajectories of the scan lines are indicated, shortened somewhat for clarity.

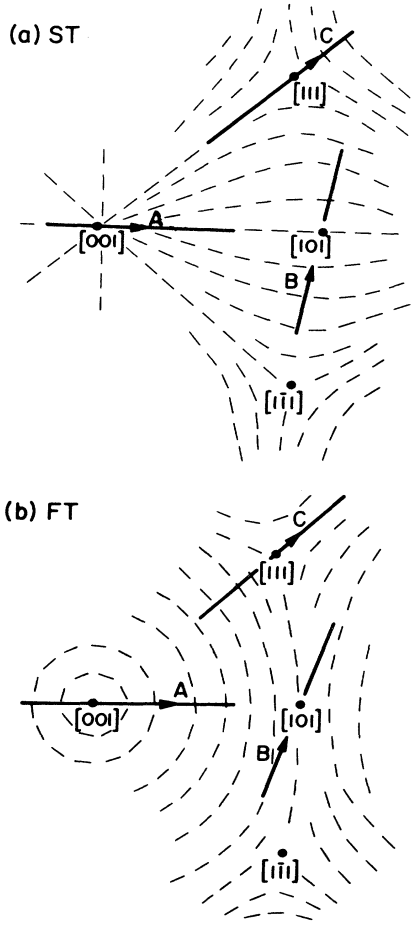

FIG. 3. Polarization patterns of the (a) ST and (b) FT modes of silicon. The approximate trajectories of the scan lines are indicated.

by the action of the piezoelectric sensor, which responds principally to normal displacements of the sensed surface, which are only excited by SV waves. Hence, only L and ST waves are detected. Moreover, for the (100) surface, on reflection L and ST waves do not mode convert with FT waves, and so the selectivity effect carries over into the multipass and head waves, and consequently there is no discernible presence of FT waves in the scan image at all. We will discuss mode selectivity further in each particular case.

A. Si(100) results

Figure 4(a) shows a measured scan image for the (100)-oriented silicon crystal A. The scan line is in the [001] direction, extending from 4 mm on one side of the epicenter to 36 mm on the other side. Figure 4(b) shows the corresponding Monte Carlo simulation incorporating all L and ST single- and multiple-pass wave arrivals including mode conversion sequences up to five passes, and also the $L \rightarrow$ST head-wave arrival. These predicted wave arrivals match up to within $\approx 1\%$ with the signal onsets in Fig. 4(a). In the measured scan image there is no discernible presence of FT waves whatsoever. The reason for this, as pointed out earlier, is that the FT waves that would contribute a signal are almost totally SH in character, and so are not excited by the thermoacoustic source and would not be detected by the transducer even if they were. We have done calculations in which the source and detector selectivity is accommodated by giving each ray a weighting equal to p^4, where p is the projection of the polarization vector of the wave in the sagittal plane (the rationale being that the amplitude is reduced by a factor p and the intensity by a factor p^2 by the source, with similar factors required for the detector). We find that this does indeed reduce the FT signal to negligible amplitude in spite of the fact that the FT waves are strongly focused towards the scan line. There are also no FT reflected waves and no $L \rightarrow$FT head wave visible in the scale image.

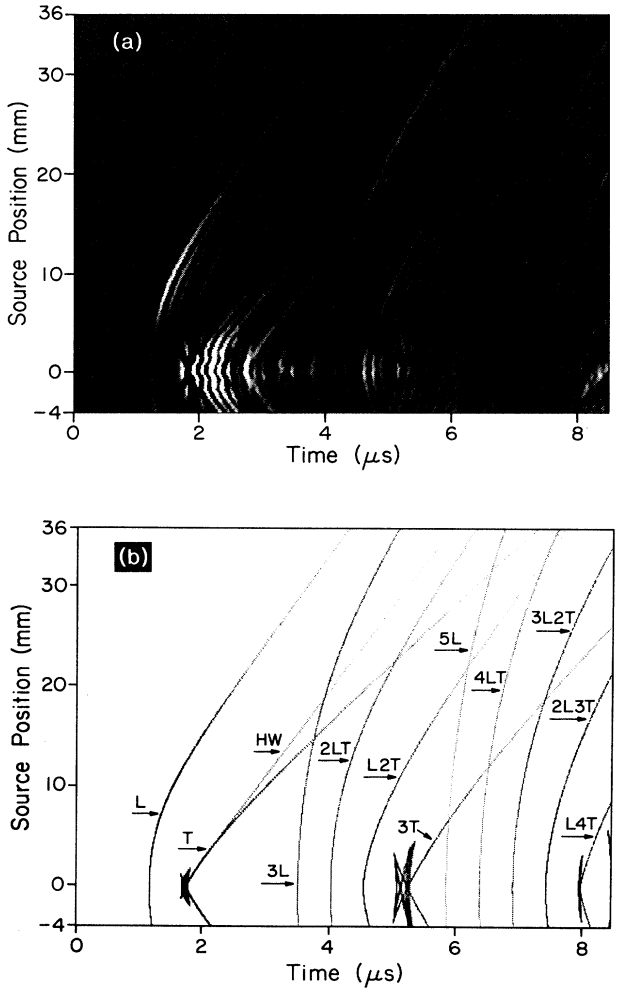

FIG. 4. (a) Measured scan image for (100)-oriented silicon crystal A. (b) Monte Carlo simulation of L and ST single- and multiple-pass wave arrivals and head wave.

The most striking feature in both the measured and the simulated scan images is the very intense ST structure near epicenter. This arises from the intense ST focusing that occurs in Si near the ⟨100⟩ directions, i.e., the "box-like" structure at the center of Fig. 2(b). This is a prominent structure in the phonon focusing patterns of many cubic crystals.[27] At its maximum, the ST signal is ≈ 30 times greater than it is in other directions where there is compensatory defocusing. This corresponds to an intensity ratio of three orders of magnitude, which is comparable to, if not greater than, the intensity enhancements encountered in phonon imaging.

Anisotropy focusing is much less pronounced for the L modes and can only partly explain the variation of the L-mode amplitude evident in Fig. 4(a). Between the epicenter (the [100] direction) and 10-mm off epicenter (the [110] direction) the increase in the L-wave amplitude predicted on the basis of focusing is $A^{1/2}(\langle 110 \rangle)/A^{1/2}(\langle 100 \rangle) = 2.29$, whereas the observed value is ≈ 14. The more important influence on the L-wave amplitude is source directivity. For a thermoacoustic source represented as crossed dipoles in the surface, the L far-field term is positive and vanishes at the epicenter, whereas the intermediate field term is negative and has a broad maximum at the epicenter. Neither of these two on its own fully explains the observed results; rather, it appears the sensor responds to a combination of the two. The T modes show little evidence of surface directivity, mainly, it would appear, because of the obscuring effect of strong focusing.

The multipass structures are all in good agreement with experiment, particularly with regard to the arrival times. We have not tried to account in detail for the amplitudes of all of these signals. This would require a better understanding of source directivity and would involve calculating the mode conversion ratios at reflections. A striking feature in the multipass signals is the $3T$ structure near the epicenter. While all the other multipass structures are convex, this one is concave, and, moreover, it terminates abruptly a few mm off epicenter.

This structure arises from the folded shape of the ST sheet of the wave surface near the [100] direction (see Fig. 1). The single-pass ST signal has a similar structure near the epicenter, but it is not as well resolved in Fig. 4(a).

At about 4 mm ($\approx 20°$) from the epicenter the $L \rightarrow$ST head-wave arrival, labeled HW in Fig. 4(b), emerges smoothly from the ST wave. In Fig. 4(a), at large angles, the head wave can be clearly discerned, though the ST wave is not visible. The ST wave near the epicenter and the head wave beyond 20° evolves smoothly into one another, giving the impression of being a single structure. This smooth transfer of signal amplitude from T wave to head wave with increasing angle is also observed in isotropic solids.[28]

Near the epicenter, at later times, there are signals due to L waves reflected off the specimen edge [the structures cutting diagonally across the lower right-hand corner of Fig. 4(a)]. We have not included edge reflections in our simulations but have carried out calculations to confirm this identification.

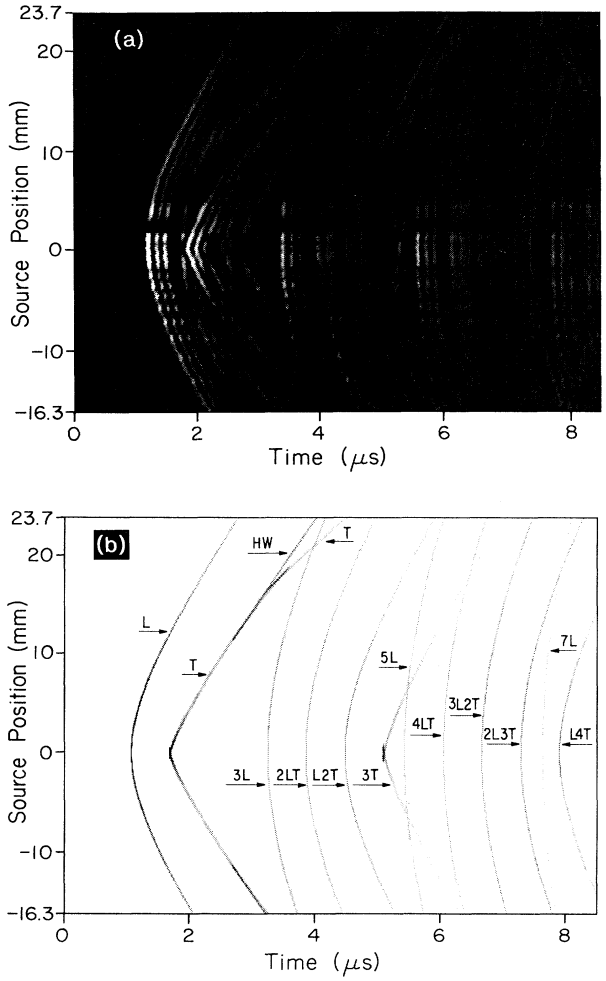

FIG. 5. (a) Measured scan image for (110)-oriented silicon crystal B. (b) Monte Carlo simulation of L and FT single- and multiple-pass wave arrivals and head wave.

B. Si(110) results

Figure 5(a) shows an experimental scan image for the (110)-oriented silicon crystal B. The scan line is in the $[1\bar{1}2]$ direction, extending from 16.3 mm on one side of the epicenter to 23.7 mm on the other side.

For this crystal orientation and scan direction, it is the FT modes that are almost completely SV in character and the ST modes that are predominantly SH in character. As a result, there is no discernible presence of ST waves in this scan image. In a Monte Carlo calculation, giving the rays a weighting p^4, as described earlier, results in the almost complete extinction of the ST-wave arrival.

Figure 5(b) shows a Monte Carlo simulation combining L and FT single- and multiple-pass wave arrivals, including mode conversions, and also the $L \rightarrow$FT head-wave arrival. The head wave is only present at fairly large angles towards the edges of the scan image. The simulated and measured scan images are in good agreement with regard to all these wave arrivals.

The strongest focusing of the FT waves occurs at epicenter in the [110] direction, where the scan line passes through a FT focusing ridge [see Fig. 2(a)]. The L-wave amplitude is negative and shows a significant decrease near the epicenter. This would indicate the surface directivity has an important affect on the L waves. Edge reflected L-wave arrivals are evident towards the right-hand side of the scan image.

The set of intense bands that run across the scan image arise from the presence of surface damage in the form of a series of small ablation pits. When the laser strikes one of these pits, a larger signal amplitude results. This can partly be attributed to the reduced optical reflectivity of the surface at the pits. Also, the L-wave amplitude is greatly enhanced relative to that of the T wave there, and this effect carries over to the $3L$, $5L$, and even $7L$ wave arrivals, which are much more prominent than the other multipass signals. It appears that some of the laser energy penetrates via the pits into the interior of the sample, where it functions as a buried thermoacoustic source, generating pure L waves. For such a source, the intermediate and far-field terms both have a maximum at the epicenter. Moreover, both are positive, corresponding to motion away from the source. This appears to be the reason for the reversal of polarity in the precursor signal to the main L signal onset. It is possible that part of the excitation is due to the expulsion of air and loose debris from the pits when the laser beam strikes. The resulting reaction force would be normal to the surface, and this would also account for the strong positive L-wave radiation in the epicentral direction.

At the ablation pits the precursor wave arrives up to ≈ 0.4 μs ahead of the main L-wave signal. We infer from this that the ultrasonic generation is taking place at distances of up to ≈ 4 mm below the surface of the sample. This gives an indication of how deep the damage, or at least some modification of the material's properties, extends. These observations demonstrate the potential usefulness of scan imaging as a tool for surface characterization.

C. Si(111) results

Figure 6(a) shows a scan image measured for the (111)-oriented silicon crystal *C*. The scan line is in the $[11\bar{2}]$ direction, extending from 20 mm on one side of the epicenter to 20 mm on the other side. Evident in this scan-image, in addition to the wave arrivals, which we will be discussing, there is a prominent *low*-frequency signal, which coincides approximately with the *L*-wave arrival at the epicenter and trails progressively further behind it away from the epicenter. We have investigated several possible mechanisms for this feature, but at present we are not able to satisfactorily explain it. Since this feature is not central to our treatment of wave arrivals, we will discuss it no further here. Interestingly, in the upper half of the measured scan image there are features that correspond to the predicted *L*- and FT-wave arrivals, but there is no visible indication of the ST-wave arrival. Conversely, in the lower half of the scan image there are features corresponding to the *L* and ST wave arrivals, but there is no visible FT signal. The explanation for this remarkable dichotomy is provided by Fig. 3. The scan line *C* passes through the [111] conical point where the polarization fields of the transverse modes possess a singularity, both undergoing abrupt 90° rotations there. For the first half of the scan line the ST modes are almost totally SV in character and the FT modes are SH, while for the second half of the scan line it is the FT modes that are SV in character and the ST modes are SH. Figure 6(b) shows a Monte Carlo simulation in which the single-pass rays it contains have all been given weightings of p^4, as described earlier, and this has the expected affect of almost totally suppressing the FT waves in the lower half and the ST waves in the upper half of the scan image.

Both the longitudinal and transverse waves clearly show the effects of anisotropy focusing. The ST signal is large throughout the lower half of the scan image, where the scan line passes within a region of strong ST focusing. The FT signal is greatly enhanced in a narrow region about 7 mm ($\approx 35°$) beyond the epicenter. This is where the scan line intersects the intense FT focusing ridge in the vicinity of the [110] direction. In the simulated scan image this focusing structure heavily saturates the gray scale because it is so narrow and intense. More obvious is the kink in the wave arrival at that point.

In contrast to the (100) and (110) scan images, the amplitude of the *L*-wave signal in the measured (111) scan image is asymmetric about the epicenter, and this provides a means of separating anisotropy focusing from source directivity, spatial attenuation, and surface projection effects, since the latter effects are to a fair approximation symmetric about the epicenter. By taking the ratio of the *L*-wave amplitude at a distance x beyond the epicenter to that at the same distance before epicenter, focusing is separated from those other effects. The experimental and predicted values of this ratio as a function of x are in fairly good agreement.

Figure 6(b) also contains predicted multipass wave arrivals and head waves. Polarization selectivity has been brought into these calculations by eliminating the transverse wave with the smaller sagittal polarization for each value of $s_{\parallel}$. The outcome of this, is that in the lower half of the scan image, there is an $L \rightarrow$ST head wave but no $L \rightarrow$FT head wave, and the multipass waves are combinations of *L* and ST waves only. Likewise, in the upper half of the scan image there is only the $L \rightarrow$FT head wave, and the multipass waves are made up of *L* and FT waves only.

In the lower portion of the simulated scan image, the $L \rightarrow$ST head wave splits off smoothly from the ST wave at about 10 mm ($\approx 45°$) from epicenter. There is a very clear feature in the measured scan image that matches up well with this predicted arrival of the head wave. As is the case for the (100) and (110) samples, the *T* wave is too small in amplitude to be observed once the head wave has formed. There is no feature in the lower half of the experimental scan image that can be interpreted as an $L \rightarrow$FT head wave. In the upper portion of the simulated scan image, the $L \rightarrow$FT head wave splits off smoothly from the FT wave at about 7 mm ($\approx 35°$) from the epi-

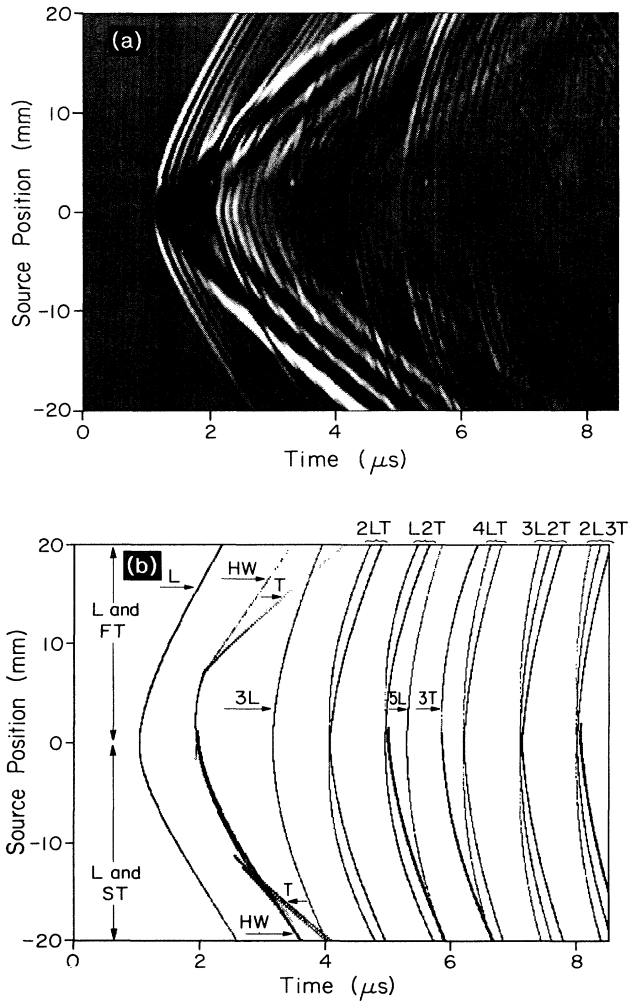

FIG. 6. (a) Measured scan image for (111)-oriented silicon crystal *C*. (b) Monte Carlo simulation of polarization selected *L* and *T* single- and multiple-pass wave arrivals and head waves.

center. In the experimental scan image there is a distinct feature that matches up with the $L \rightarrow$FT head wave. Again, the T wave disappears once the head wave has formed. There is no $L \rightarrow$ST head wave in this region of the scan image.

Because the (111) reflecting surfaces are not parallel to a crystallographic mirror plane, for any given value of $\mathbf{s}_{\parallel}$, the L waves traveling towards the detector and source surfaces are not equivalent. They do not yield the same transit time nor lateral displacement. Similar comments apply to the T waves. This leads to a greater multiplicity of multipass waves, although there are still some equivalences that remain. The $\mathbf{V}^{+}$ rays can still be permuted among themselves and the $\mathbf{V}^{-}$ rays among themselves. The consequence of this is that there is a twofold splitting of the $2LT$, $L2T$, $4LT$, and $L4T$ wave arrivals and a threefold splitting of the $3L2T$ and $2L3T$ wave arrivals. These patterns of splittings show up clearly in Fig. 6(b). Because of the large number of multipass wave arrivals, each trailing their individual ringing patterns, which tend to overlap, individual wave arrivals are more difficult to distinguish from each other for this crystal orientation than for the others. Nevertheless, there is a fair measure of agreement between simulation and experiment regarding these waves. A few of the multipass wave arrivals show up distinctly, and elsewhere the arrival of signals in the scan image conform reasonably well to prediction. The problem of identifying multipass waves for a completely general scan image where all three modes are present in all directions, would undoubtedly be much more difficult.

There is one point where the scan line passes through an ablation pit in the surface, giving rise to the narrow intense band slightly above the epicenter in Fig. 6(a). Here there is stronger L-wave generation, and this enhancement carries over to the $3L$, $5L$, and even $7L$ wave arrivals, providing a kind of calibration strip. The $3L$ and $5L$ signals are in good agreement with their predicted wave arrivals. Edge reflected L-wave arrivals are again evident towards the right-hand side of the measured scan image.

V. CONCLUSIONS

Using a scanned ultrasonic point-source–point-receiver technique on single crystals of silicon we have observed pronounced anisotropy focusing in the amplitudes of transverse-wave arrivals and, to a lesser extent, longitudinal waves. These results are a clear experimental demonstration of phonon focusing of MHz ultrasonic waves. The main features in our results are well accounted for in Monte Carlo simulations based on ray constructs.

The scan images of silicon we have obtained contain a multiplicity of structures due to multipass modes, incorporating mode-conversion effects. Mode selectivity has been shown to come about through the specific nature of the polarization fields of the transverse modes and the symmetry of the generation mechanism. Our scan images of silicon also display well defined structure due to the passage of $L \rightarrow$ST and $L \rightarrow$FT head waves.

We have shown that the presence of surface damage has a marked effect on the wave forms that are generated. We have been able to infer from the observed changes that the damage alters the generation mechanism, and we have been able to estimate from the time dependence of the signals how far the damage penetrates into the interior of the material.

The method described here is in some regards complementary to conventional phonon imaging. It does not offer the high sensitivity and spatial resolution of phonon imaging; its advantage lies rather in its access to materials and conditions not suitable to phonon imaging. It is a room-temperature technique, which can be applied to a wide range of materials including metals and fiber-reinforced composites, in which ballistic phonon propagation does not occur. Moreover, it provides good time resolution, which allows for the accurate determination of elastic constants and other material properties. We have also demonstrated the usefulness of this method as a tool for surface characterization.

ACKNOWLEDGMENTS

This work has been supported by the NSF-funded Materials Science Center at Cornell University. A.G.E. also acknowledges support from the University of the Witwatersrand; W.S. acknowledges the support of the U.S. Office of Naval Research (ONR), M.O. Thompson is thanked for making available the laser, which was used in the experiments. K.Y. Kim, R. L. Weaver, and J. P. Wolfe are thanked for helpful discussions.

*On leave from the University of the Witwatersrand, P.O. Wits 2050, South Africa.

[1]A preliminary report on these findings has been published: A. G. Every, Wolfgang Sachse, K. Y. Kim, and M. O. Thompson, Phys. Rev. Lett. **65**, 1446 (1990).

[2]W. Sachse and K. Y. Kim, in *Review of Quantitative Nondestructive Evaluation,* edited by D. O. Thompson and D. E. Chimenti (Plenum, New York, 1986), Vol. 6A, p. 311; also in *Ultrasonic Materials Characterization II,* edited by J. Boussiere, J. P. Monchalin, C. O. Ruud, and R. E. Greene (Plenum, New York, 1987), p. 707.

[3]H. J. Maris, J. Acoust. Soc. Am. **50**, 812 (1971).

[4]A. K. McCurdy, H. J. Maris, and C. Elbaum, Phys. Rev. B **2**, 4077 (1970); B. Taylor, H. J. Maris, and C. Elbaum, *ibid.* **3**, 1462 (1971).

[5]H. J. Maris, in *Nonequilibrium Phonons in Non-Metallic Crystals,* edited by W. Eisenmenger and A. A. Kaplyanskii (North-Holland, Amsterdam, 1986), p. 51.

[6]F. Rosch and O. Weis, Z. Phys. B **25**, 101 (1976); **25**, 115 (1976).

[7]G. A. Northrop and J. P. Wolfe, Phys. Rev. B **22**, 6196 (1980).

[8]P. Taborek and D. L. Goodstein, Phys. Rev. **B22**, 1550 (1980).

[9]G. A. Northop and J. P. Wolfe, in *Nonequilibrium Phonon Dynamics,* edited by W. E. Bron (Plenum, New York, 1985), p. 165.

[10]H. Schreyer, W. Dietsche, and H. Kinder, in *LT-17,* edited by

U. Eckern, A. Schmid, W. Weber, and H. Wuhl (North-Holland, Amsterdam, 1984), p. CR 4.
[11]A. N. Ceranoglu and Y. H. Pao, ASME J. Appl. Mech. **48**, 125 (1981); **48**, 133 (1981); **48**, 139 (1981).
[12]M. J. P. Musgrave and R. G. Payton, Quart. J. Mech. Appl. Math. **34**, 235 (1981); **35**, 173 (1982).
[13]D. A. Hutchins, in *Physical Acoustics,* edited by W. P. Mason and R. N. Thurston (Academic, Boston, 1988), Vol. XVIII, p. 21.
[14]C. B. Scruby, R. J. Dewhurst, D. A. Hutchings, and S. B. Palmer, in *Research Techniques in Nondestructive Testing,* edited by R. S. Sharpe (Academic, New York, 1982), Vol. 5, p. 281.
[15]K. Aki and P. G. Richards, *Quantitative Seismology* (Freeman, San Franciso, 1980), Vol. 1.
[16]G. F. D. Duff, Philos. Trans. R. Soc. London **252**, 249 (1960).
[17]V. T. Buchwald, Proc. R. Soc. A **253**, 563 (1959).
[18]F. R. Yeatts, Phys. Rev. B **29**, 1674 (1984).
[19]N. Cameron and G. Eason, Quart. J. Mech. Appl. Math. **20**, 23 (1967).
[20]R. G. Payton, *Elastic Wave Propagation in Transversely Isotropic Media* (Martinus Nijhoff, The Hague, 1983).
[21]M. R. Karim and A. K. Mal (unpublished).
[22]B. A. Auld, *Acoustic Fields and Waves in Solids* (Wiley, New York, 1973), Vol. 1.
[23]M. J. P. Musgrave, *Crystal Acoustics* (Holden Day, San Francisco, 1970).
[24]J. F. Nye, *Physical Properties of Crystals* (Oxford University Press, London, 1957).
[25]J. D. Aussel, A. Le Brun, and J. C. Baboux, Ultrasonics **26**, 245 (1988).
[26]The elastic constants and density for the calculations on silicon were taken from Ref. 22: $C_{11}=165.7$, $C_{12}=63.9$, $C_{44}=79.56$ GPa, and $\rho=2332$ kg/m^3.
[27]A. G. Every, Phys. Rev. B **24**, 3456 (1981); D. C. Hurley and J. P. Wolfe, *ibid.* **32**, 2568 (1985).
[28]U. Schleichert, K. J. Langenberg, W. Arnold, and S. Fabbender, in *Review of Quantitative Nondestructive Testing,* edited by D. O. Thompson and D. E. Chimenti (Plenum, New York, 1989), Vol. 8A, p. 489.

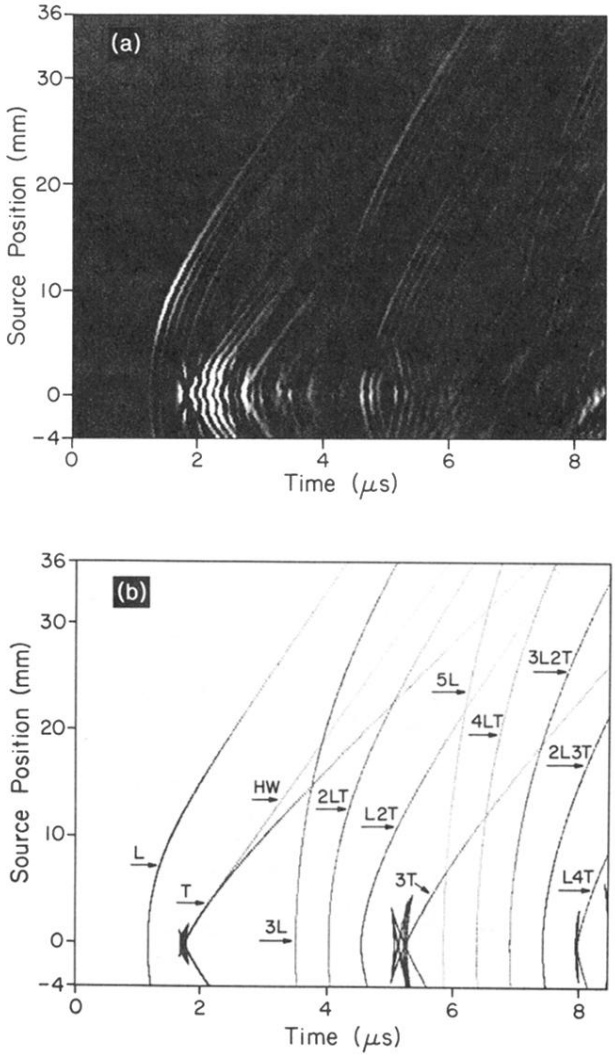

FIG. 4. (a) Measured scan image for (100)-oriented silicon crystal *A*. (b) Monte Carlo simulation of *L* and ST single- and multiple-pass wave arrivals and head wave.

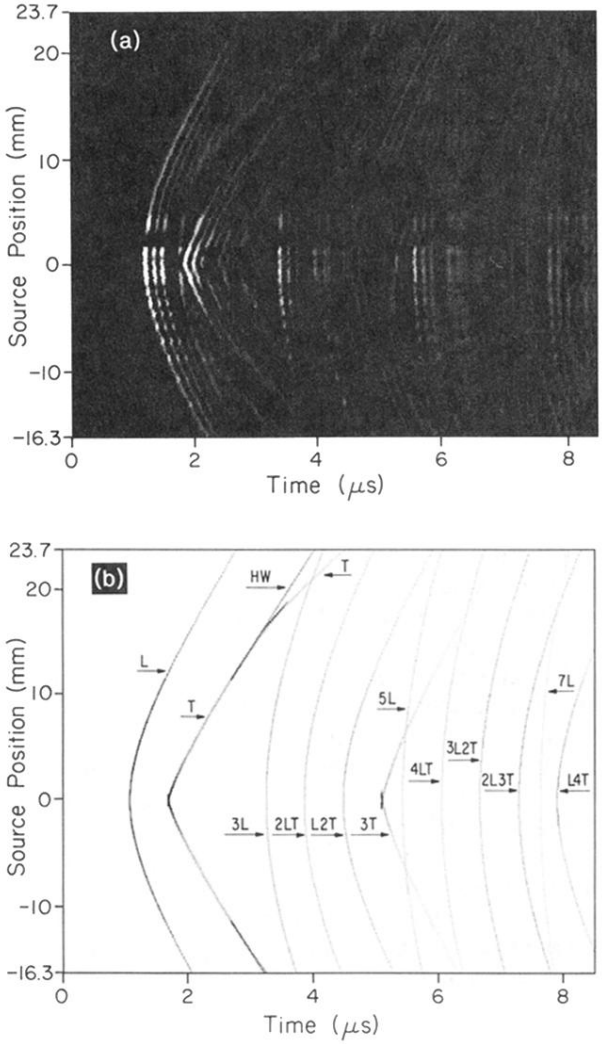

FIG. 5. (a) Measured scan image for (110)-oriented silicon crystal *B*. (b) Monte Carlo simulation of *L* and FT single- and multiple-pass wave arrivals and head wave.

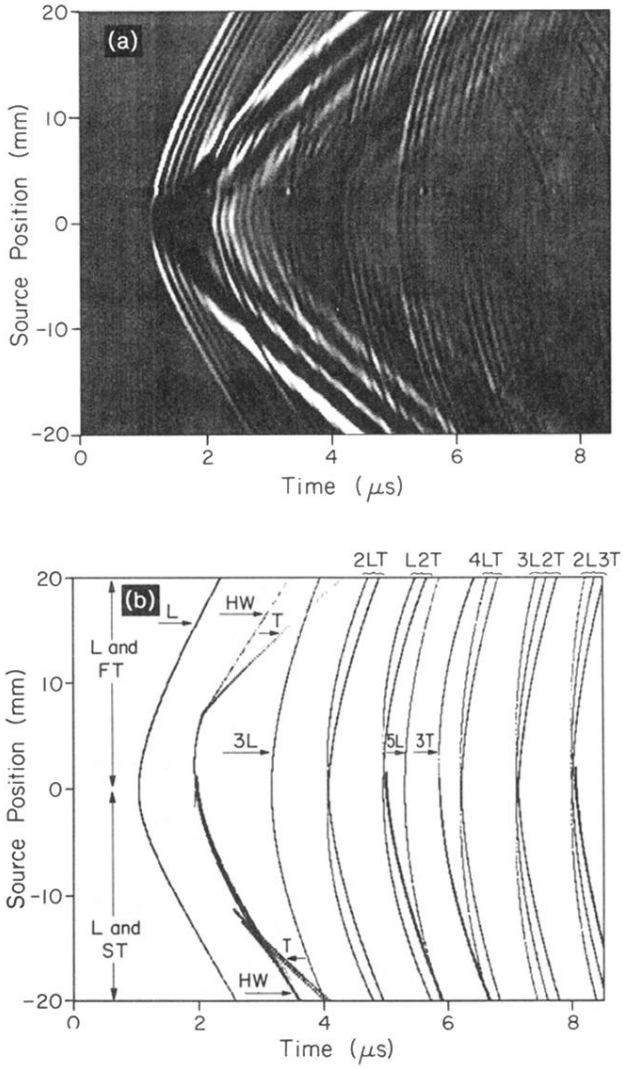

FIG. 6. (a) Measured scan image for (111)-oriented silicon crystal *C*. (b) Monte Carlo simulation of polarization selected *L* and *T* single- and multiple-pass wave arrivals and head waves.